MODELING GRAIN BOUNDARY ANISOTROPY-DRIVEN MICROSTRUCTURAL EVOLUTION WITH ARBITRARY GRAIN ORIENTATION AND ADAPTIVE MESH REFINEMENT

by

JOSEP MARIA GRAS RIBOT

B.S., Universitat Politècnica de Catalunya, 2016

A thesis submitted to the Graduate Faculty of the

University of Colorado Colorado Springs

in partial fulfillment of the

requirements for the degree of

Master of Science

Department of Mechanical and Aerospace Engineering

[2018]

© 2018

JOSEP MARIA GRAS RIBOT

ALL RIGHTS RESERVED

This thesis for the degree of Master of Science by

Josep Maria Gras Ribot

has been approved for the

Department of Mechanical and Aerospace Engineering

by

Brandon Runnels, Chair

Xin (Cindy) Wang

Todd Bredbenner

Date: May 7, 2018

Gras Ribot, Josep Maria (M.S. Mechanical Engineering)

Modeling grain boundary anisotropy-driven microstructural evolution with arbitrary grain orientation and adaptive mesh refinement

Thesis directed by Professor Brandon Runnels

ABSTRACT

The development of new technology requires new materials with designed properties for high performance applications. This next generation of materials must be lighter, stronger and with the rest of their properties well characterized. Of particular interest for their wide range of applications are crystalline materials, in particular, metals. Recent efforts have been made to move towards nanodesigned materials, but in order to nanodesign materials their microscopic and mesoscopic properties have to be understood and well defined. Interfaces in crystalline materials are key players in a variety of mesoscopic and microscopic processes such as solidification, recrystallization, severe plastic deformation and grain boundary migration, stability and twinning. Of particular interest among all kind of interfaces are grain boundaries. Their simple geometry allows to generate a computational compact frameworks for their study.

The aim of this work is to increase the understanding of crystalline materials by computationally modeling the effect of anisotropic grain boundary energy on boundary formation, faceting, and migration. To examine the effect of strong energetic anisotropy, highly nonconvex energy functions are used. These energy functions exhibit strong cusps, both with and without continuous derivatives, to accurately replicate realistic boundary energy. This energy function without continuous derivatives is similar to that generated with the latest molecular dynamics simulations and other approaches, which are believed to be accurate in defining boundary energy. In this work, a simplified 2D interface between metals is considered. The boundary energy is coupled with Cahn-Hilliard kinetics in a phase field

model with diffusive (finite width) boundaries. The developed phase field model can be easily coupled with other mechanical or thermal mechanisms, providing a framework that would allow the study of the coupling of grain boundaries with these phenomena. The present work is a major step towards developing the necessary computational framework to understand the behavior and the kinetics of grain boundaries.

ACKNOWLEDGEMENTS

Pursuing a masters degree at the UCCS would not have been possible without the opportunity given by the Balsells foundation through the Balsells Mobility and Fellowship programs. Therefore, I want to thank Mr. Pete Balsells for creating these programs and giving the opportunity to catalan engineering students to study in the United States.

I want to thank my advisor Dr. Runnels, for all the support, patience and guidance during these two and a half years.

I also want to thank Dr.McGuirk and Dr. Adams, for giving me the opportunity to work as a lab instructor. Life at UCCS would not have been the same without this teaching experience.

I want to thank my friends Carles and Monica, alway there when needed, specially in the times of stress or struggle.

Last but not least, I want to thank my family, for all the support and encouragement that crossed the ocean.

CONTENTS

CHAPTER

I. INTRODUCTION 1

II. THE REGULARIZED PHASE FIELD METHOD 7

Phase field modeling of microstructure 7

Evolution equation (3D) 9

Evolution equation (2D) 11

III. COMPUTATIONAL IMPLEMENTETION 13

Grain boundary energy modeling 13

Implementation 14

Numerical integration and stability 14

Performance 16

IV. ANALYSIS 18

Numerical interface parametrization 18

Frequency analysis 19

Slope analysis 20

V. RESULTS 21

Effect of boundary energy function and curvature energy 21

Versatility of the PF method 23

Evolution and convergence of the interface 23

Analysis of corner energy magnitude 23

VI. CONCLUSIONS AND FUTURE WORK 27

Conclusions 27

Future Work 28

REFERENCES 29

APPENDICES

A. VARIATIONAL DERIVATIVES (3D) 34

B. VARIATIONAL DERIVATIVES (2D) 37

LIST OF FIGURES

FIGURE

1.1. Schematic representations of a tilt boundary (left) and a twist boundary(right) between two idealized grains [9] 2

1.2. Faceted interface experimentally observed in copper [16] 2

1.3. Analysis between the relationship of convex functions and faceting [24] . . 5

2.1. PF model for a crystalline microstructure (top) and PF parameters over a path (bottom) [9] 8

2.2. Schematic representation of the eigenvectors of a surface and the principal curvatures [33] 11

3.1. Comparision of smooth and nonsmooth energy functions. 14

3.2. Results from a phase field test showing the 3 levels of mesh refinement, and how the interface is constrained to the finer level. 15

3.3. Numerical five-point stencil for a 4th order derivative 16

4.1. The original diffuse boundary (left) is processed using VisIt and results in a grayscale image (center). Python is used to parameterize the boundary characterized by the level set $\eta = 0.5$ (right). 18

4.2. Fast Fourier transformation of the interface at a concrete time step, the higher the intensity is for a frequency, the more dominant it is on the interface. 19

4.3. Fourier analysis of interface convergence as a function of time. 20

5.1. Qualitative comparison of experimental and computational results of energy anisotropy-driven microstructure evolution. The faceting behavior of the interface under annealing is replicated. 22

5.2. Comparison of both boundary energy functions (σ_{gb_I} and $\sigma_{gb_{II}}$) with the same magnitude for all the PF parameters, $\sigma_0 = 0.15,\ \sigma_1 = 0.95,\ \beta = 0.0001,\ \ell_{gb} = 0.05$. A difference in the facet junction curvature due to the different boundary energy is observed. 22

5.3. Interface evolution under different GB parameters. The versatility of the PF model and the variety of equilibrium configurations is observed 23

5.4. Spectral convergence analysis of interface indicating that the uniform facet configuration is stable. 24

5.5. Analysis of the effect of the rate σ_1/β for $\ell_{gb} = 0.1$ 25

5.6. Analysis of the effect of the rate σ_1/β for $\ell_{gb} = 0.08$ 25

5.7. Analysis of the effect of the rate σ_1/β for $\ell_{gb} = 0.1$ 26

LIST OF TABLES

TABLE

3.1. Δt for several values of β and Δx 16

CHAPTER I

INTRODUCTION

Materials are crucial to the development of modern technology. Structural materials with a high strength to weight ratio have many applications, such as military body armor and space vehicles structure and armor. Materials with a high thermal and electric conductivity are needed for the next generation of chips and other computer science applications. Most of the materials used for the mentioned applications are crystalline materials. Crystalline materials are solid materials in which their constituents (atoms, molecules or ions) are arranged in a highly ordered microscopic structure, called crystal lattice. Crystalline materials usually are organized in different grains. A grain or crystallite is a set of atoms that form part of the same crystal lattice. The properties and performance of crystalline materials is affected by the interfaces between the different grains of the material. Interfaces are key players in processes such as solidification, recrystallization, severe plastic deformation and grain boundary stability migration and twining. Interfaces also drive important properties of the materials such as thermal and electrical conductivity and strength against supersonic impacts. Of particular interest are faceted interfaces, present both in empirical observation and in recent molecular dynamics simulations [1]. Faceted interfaces are of great influence in phenomena such as deformation twinning [2], interface sliding under deformation [3], interface mobility [4, 5, 6, 7] and solidification [8]

Grain boundaries (GB) are a particular case of interface between grains formed by the same crystalline material in the same phase and crystal structure. The atoms in a grain can be classified by bulk or relaxed atoms and surface or boundary

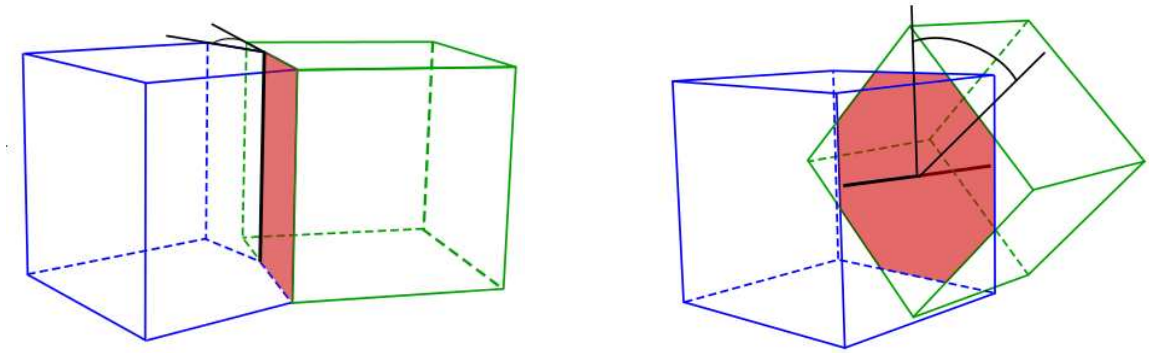

Figure 1.1: Schematic representations of a tilt boundary (left) and a twist boundary(right) between two idealized grains [9]

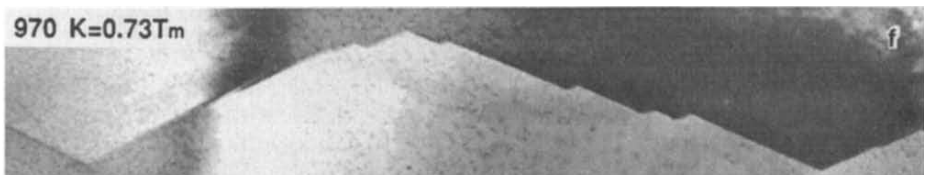

Figure 1.2: Faceted interface experimentally observed in copper [16]

atoms. The bulk atoms have minimum potential energy, and are therefore energetically stable. Boundary atoms are not in a minimum potential energy state; due to their disordered structure, they exhibit an excess of free energy, and are said to be in metastable equilibrium. This excess of potential energy can drive the migration of the GB under the proper conditions.

The interfacial energy of a GB depends on the inclination of the adjacent grains and the orientation of the interface, and is defined over a space parameterized by 5 degrees of freedom (DOF). Of these 5 DOF, 3 are due to the rotation relationship between the two crystal lattices and 2 are defined by the orientation of the interface.

Anisotropic (orientation dependent) models to determine the equilibrium shape of the crystals date from more than a century ago [10, 11, 12]. Wulff determined the equilibrium shape of a crystal inclusion given the GB energy profile [10]. This approximation to the equilibrium shape, known as the Wulff's construction forms the basis for the previous work on grain boundaries and crystal interfaces [13, 14, 15].

GBs commonly exhibit a hill-and-valley structure in crystalline materials (Figure 1.2). This structure can be understood as a consequence of the boundary energy. The boundary energy is usually nonconvex and strongly orientation dependent, and have "cusps" or minima for special orientations [17]. Convex functions are those where the line segment between any two points of the graph lies above or on the graph. If a function is nonconvex, then the minimum of that function become points of equilibrium. A common example of the consequence of nonconvexity can be seen in the functional $I : C_0([0,1]) \to R^+$

$$I[u] = \int_0^1 f(u, u')dx = \int_0^1 \Big((u'(x)^2 - 1) + u^2(x)\Big)dx. \tag{1.1}$$

We see that $I \geq 0$ for all u, so a function u such that $I[u] = 0$ is a minimizer of I. But such a u does not exist. From the second part of the integrand we get that the minimizer must be $u(x) = 0$. But from the right part we see that a minimizer must also satisfy $u'(x) = \pm 1$ for all $x \in [0,1]$. This indicates that f is nonconvex in its second argument (Figure 1.3a). We see that these two competing terms drive the minimizing function to create infinitesimally small facets with slope ± 1, but arbitrarily small value that is

$$\lim_{z \to 0} \inf I[z] = 0, \tag{1.2}$$

(Figure 1.3b). Thus, it is impossible to solve the problem as it is ill-posed.

This nonconvex form of the GB energy induces instability under microscopic perturbations of the interface. Under the proper thermodynamic conditions, if a GB is not oriented in a minimal energy configuration it will tend to migrate to a hill-and-valley structure that is energy-minimizing, even if the total interface area is increased [18, 19].

The interface energy problem has been approached with different methods. In the present work, a variational approach is used. Variational methods solve the extremal functions (maximums or minimums) for a problem with the form $F = \int f dx$, where f is a functional (function of functions). Materials tend to behave in such a way as to minimize their energy, therefore variational methods are

useful as they give a energy minimizing formulation applicable to the GB problem. Variational methods allow a formulation of the model using generalized degrees of freedom, decoupling the material physics from the kinematics and geometry of the system, therefore having a general expression applicable in all the domain. For GBs the functional f is the boundary energy, and the variational methods derive a solution for minimum energy configuration.

There have been several approaches to model the evolution of GBs. Molecular dynamics simulations have yielded comprehensive results for the microscopic properties of the GB, but the computational cost is extremely high. For mesoscale modeling, a promising computational approach is the phase field (PF) method. The PF method enables the tracking of several phases or configurations at the same time by introducing a field variable for each of the phases, and can be supplemented with data obtained from molecular dynamics simulations or analytic models. Furthermore, the computational cost of PF is relatively low. PF method has been previously used to try to solve the problem of grain growth and migration [20, 21, 22, 23]. A significant effort has been made by Moelans et al. to link the PF parameters with the GB physical properties [21, 20]. Real GBs are non-diffuse, but for numerical purposes and stability, a diffuse approach is needed for stability. PF also has been used with anisotropic properties for the GBs. Kazaryan et al. developed an anisotropic scheme to solve for the boundary energy and mobility, that showed that the mobility anisotropy does not have an effect on the equilibrium shape of the GB, while the boundary energy induces the equilibrium shape of the interface [23].

The boundary energy problem is ill-posed because of the high nonconvexity of the GBs energy functions (Equations 1.1-1.2, Figure 1.3). As a result, the solution is a boundary with microfacets that are theoretically infinitely small, due to a lack of length scale. To regularize this problem and set a lengthscale for the facet dimensions, some kind of second order energy penalty is needed. This second order regularization is based on the introduction of a curvature based energetic term. Some attempts to define this curvature penalty term include those by Herring [25]

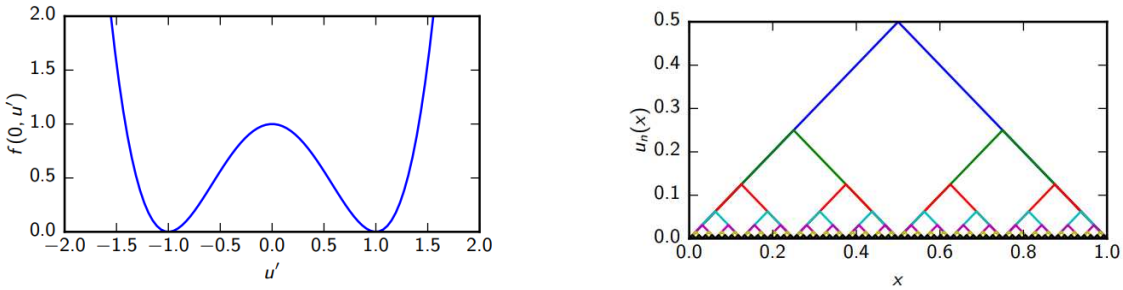

(a) (b)

Figure 1.3: Analysis between the relationship of convex functions and faceting [24]

and Mullins[26], that introduced the concept of a curvature energy proportional to the mean curvature. Di Carlo et al. developed a general regularized equation for anisotropic motion by curvature [27]. This general equation has been used by Gurtin & Jabbour [28], who developed a regularized version of the evolution equation that is a function of the curvature tensor, defined as the gradient of the normal vector to the interface. Other curvature-based regularization approaches include those by Wheeler [29] and Torabi et al. [30]. Wheeler developed a method to evaluate the edge energy and showed that it scales with the regularization, the higher the regularization the higher the associated edge energy. Torabi used the Willmore energy (proportional to the mean curvature squared) as the curvature associated energy, and was able to replicate the asymptotic shapes predicted by Spencer [31]. While both methods exhibits an effective means of regularization, the use of the mean curvature ultimately results to an inability to properly penalize saddle points. Furthermore, these methods can adversely affect other model properties such as energy and diffuse length, and are not thermodynamically consistent with the Moelans parameterization.

One of the most recent approaches is the one taken by Abdeljawad et al. [32]. This approach introduces non-local effects that account for nonlocal interactions between facet junctions. This method generated promising results, but it works only when solved using spectral space methods, which require strictly periodic boundary conditions.

In summary, despite the significant work in phase field modeling of GB, additional work is still needed to be able to robustly handle boundaries with strong nonconvex energies. In particular, a regularization method is needed that can work in spectral or real space, is physically linked to curvature, and is thermodynamically consistent with other phase field formulations.

CHAPTER II

THE REGULARIZED PHASE FIELD METHOD

2.1 Phase field modeling of microstructure

The phase field method is a mathematical model particularly useful for solving problems containing well-defined interfaces. Rather than parameterize boundaries explicitly, an auxiliary field η is used to track the boundary location. η is typically referred to as order parameter, and is evolved using a partial differential equation. In multi-phase field models, microstructure is described by set of order parameters η_i, each of which is related to a specific phase or crystallographic orientation. A phase is present in a point when its order parameter $\eta_i = 1$, when $\eta_i = 0$ the phase is not present, and when $\eta_i \in (0, 1)$ that point is in the interface (Figure 2.1). A model for a phase field can be constructed by physical arguments using an explicit expression for the free energy of the system. In the present work the free energy is the sum of all the energy contributions at the GB, described by the integrand

$$\begin{aligned} F &= \int_V f(\eta_1 ... \eta_p, \nabla\eta_1, ... \nabla\eta_p, \Delta^2\eta_1, ..., \Delta^2\eta_p) dV \\ &= \int_V \sum_i (W(\eta_1, \ldots, \eta_p) + \frac{1}{2}\kappa_i(\mathbf{n})||\nabla\eta_i||^2 + \frac{\beta}{2}C_i)) dV, \end{aligned} \tag{2.1}$$

where $W(\eta_1, \ldots, \eta_p)$ is the chemical potential, $\frac{1}{2}\kappa_i(\mathbf{n})||\nabla\eta_i||^2$ is the anisotropic boundary energy, $\mathbf{n}$ is the vector normal to the surface and $\frac{\beta}{2}C_i$ is the junction energy. The chemical potential $W(\eta_1, \ldots, \eta_p)$ is a multi-well potential with strict local minima at 0 and 1. This term restricts the solution to the admissible values of the PF order parameters.

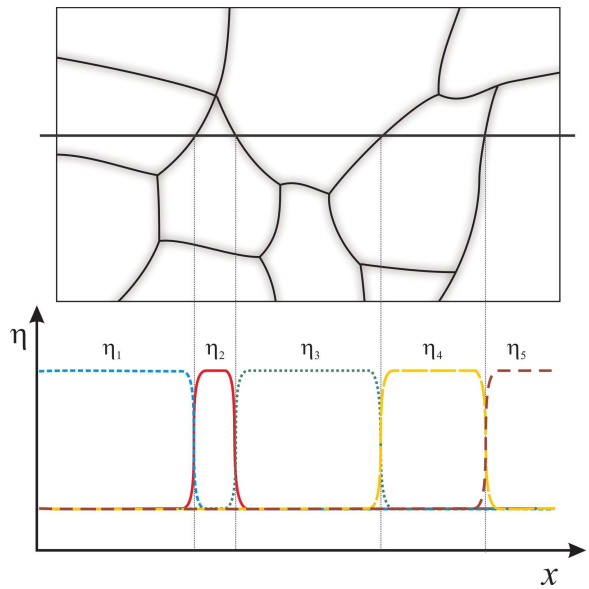

Figure 2.1: PF model for a crystalline microstructure (top) and PF parameters over a path (bottom) [9]

The parameters used are typically designed with numerical convenience in mind, but they must be described in terms of physical energetic quantities. Following Moelans et al., the PF parameters are related to physical quantities via the following relationships: [20]

$$\gamma = 1.5, \qquad \kappa(\mathbf{n}) \approx \frac{3}{4}\sigma_{gb}(\mathbf{n})\ell_{gb}, \qquad L \approx \frac{4}{3}\frac{m_{gb}}{\ell_{gb}}, \qquad \mu \approx \frac{3}{4}\frac{1}{f_{0,saddle}(\gamma)}\frac{\sigma_{gb}}{\ell_{gb}}, \tag{2.2}$$

where $\sigma_{gb}(\mathbf{n})$ is the boundary energy as a function of the normal to the interface,$f_{0,saddle}(\gamma)$ is the energy at the saddle point of the chemical potential energy, ℓ_{gb} is the diffuse boundary width and m_{gb} is the boundary mobility. γ, κ, L, and μ are model parameters.

To evolve the order parameters through time, the assumption that materials tend to minimize their energy is taken. This enables the formulation of a kinetic equation. The Allen-Cahn equation describes an L^2 gradient descent that evolves the PF order parameters in direction of minimum energy set by the variational derivative of the free energy functional. The Allen-Cahn equation has the follow-

ing form

$$\frac{d\eta_i}{dt} = -L\frac{\delta f}{\delta \eta_i}. \tag{2.3}$$

where $\delta/\delta\eta_i$ indicates a variational derivative. The evaluation of Equation 2.3 is non-trivial and will be treated explicitly in the following section.

2.2 Evolution equation (3D)

To evolve the boundary we apply the Allen-Cahn equation 2.3. With the Euler rule, the variational derivative of f becomes

$$\frac{\delta f}{\delta \eta_i} = \frac{\partial}{\partial \eta_i}(f) - \frac{\partial}{\partial x_j}\frac{\partial}{\partial \eta_{i,j}}(f) + \frac{\partial^2}{\partial x_p \partial x_q}\frac{\partial}{\partial \eta_{i,pq}}(f). \tag{2.4}$$

Depending on the form of f, the variational derivative can become quite cumbersome, and simplicity in the formulation of f is advantageous.

We begin with the chemical potential $W(\eta_1, \ldots, \eta_n)$. The following multi-well form for $W(\eta_1, \ldots, \eta_n)$ is used

$$W(\eta_1, \ldots, \eta_n) = \mu \sum_{p=1}^{n} \Big(\frac{1}{4}\eta_p^4 - \frac{1}{2}\eta_p^2 + \frac{\gamma}{2}\sum_{q \neq p} \eta_p^2\, \eta_q^2 \Big), \tag{2.5}$$

which has a highly simplified form when derivated variationally.

The boundary energy term has the following form

$$\kappa(\mathbf{n})||\nabla \eta_i||^2, \tag{2.6}$$

where $\kappa(\mathbf{n})$ is the anisotropic boundary energy and $||\nabla \eta_i||^2$ accounts for the inclination of the interface. We emphasize that $\sigma_{gb}(\mathbf{n})$ can be any function as long as there is expressions or approximations of its first and second derivatives.

The main contribution to this work is the introduction of a unique curvature term C, which has the form

$$C = \frac{1}{2}(\kappa_1^2 + \kappa_2^2), \tag{2.7}$$

where κ_1, κ_2 are the principal curvatures of the η curvature tensor. (We note that it can be shown that this measure of curvature can be alternatively defined in terms of the mean curvature $H = \frac{1}{2}(\kappa_1 + \kappa_2)^2$ and the Gaussian curvature $K = \kappa_1\kappa_2$,

$$C = 2H^2 - K^2). \tag{2.8}$$

This curvature is nonzero at saddle points and planar curves, and consequently does not exhibit the same deficiency at saddle points as the mean curvature.

The principal curvatures κ_1 and κ_2 are the 2nd and 3rd eigenvalues of the Hessian ($H_i = \nabla^2\eta_i$). From Equation 2.1, the only term that depends on the 2nd order derivatives is the curvature term. Applying this result to Equation 2.4, the only nonzero derivation from the 3rd term of the right hand side is the curvature term.

The use of eigenvalues initially presents an apparent challenge in the computation of the variational derivative. This difficulty is resolved by a simple change of basis. We notice that, if working in the eigenbasis of the Hessian (Figure 2.2), the Hessian is diagonal,

$$H_i = \nabla^2\eta_i = \begin{bmatrix} \eta_{i,11} & 0 & 0 \\ 0 & \eta_{i,22} & 0 \\ 0 & 0 & \eta_{i,33} \end{bmatrix}, \tag{2.9}$$

and κ_1 and κ_2 are simply $\eta_{i,22}$ and $\eta_{i,33}$. Thus, the variational derivative term simplifies dramatically to

$$\frac{\partial^2}{\partial x_p \partial x_q}\frac{\partial}{\partial \eta_{i,pq}}(f) = \frac{\partial^2}{\partial x_p \partial x_q}\frac{\partial}{\partial \eta_{i,pq}}(\frac{\beta}{2}C) = \beta(\eta_{i,2222} + \eta_{i,3333}).$$

It is natural to question, at this point, the legitimacy of working in the eigenbasis of an operator that may be changing through time. The resolution to this possible objection is that, because the kinetic equations are all scalar, any change of basis is allowed because it will apply to the vector operators only. This resolves any questions regarding time dependence of the change of basis operators.

Another natural objection is whether it is computationally worthwhile to find

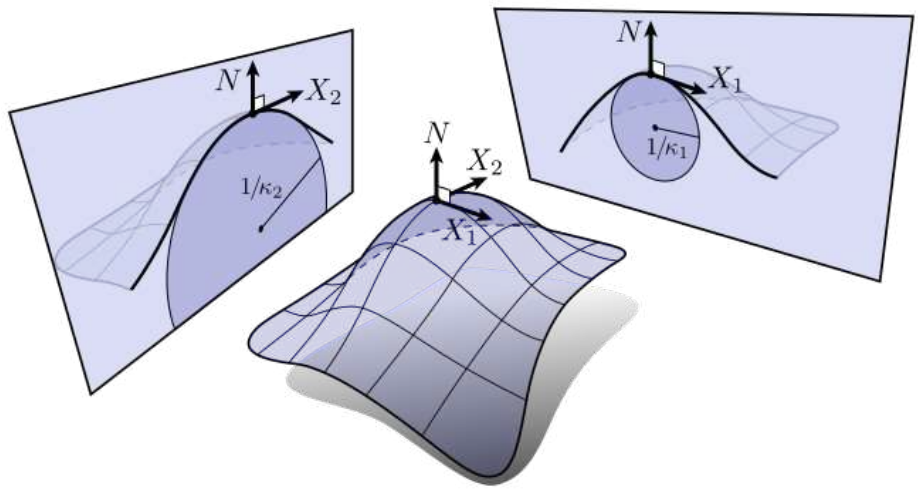

Figure 2.2: Schematic representation of the eigenvectors of a surface and the principal curvatures [33]

the eigenbasis. This is easily resolved by noticing that the first eigenvector of the Hessian is closely approximated by the interface normal $\boldsymbol{n}$, a quantity that has already been computed as

$$\mathbf{n} = \frac{\nabla \eta_i}{|\nabla \eta_i|}. \tag{2.10}$$

The remaining vectors $\mathbf{b}$ and $\mathbf{t}$ are tangential to the surface, and can easily be calculated from the Hessian.

Combining this with the results from the other terms, the following expresion forms the complete kinetic equation

$$\begin{aligned}\frac{\delta \eta_i}{\delta t} = &- L\Big(\mu\Big(\eta_i^3 - \eta_i + 2\gamma_i \eta_i \sum_{i \neq j} \eta_j^2\Big) - \Big(\frac{\partial}{\partial x_j}\Big(\frac{1}{2}\frac{\partial \kappa_i}{\partial \mathbf{n}}\frac{\partial \mathbf{n}}{\partial \eta_{i,j}}\Big) \\ &+ \sum\Big(\frac{\partial \kappa_i}{\partial n_j}(n_j - n_j^2 \sum_p n_p)\eta_{i,jj}\Big) + \kappa_i \eta_{i,jj}\Big) + \beta\Big(\eta_{i,2222} + \eta_{i,3333}\Big)\Big).\end{aligned} \tag{2.11}$$

(See Appendix A for a complete derivation).

2.3 Evolution equation (2D)

For the present work, due to the limited computational resources, instead of developing a computationally expensive 3D case, a 2D approach is studied. The 2D

case evolution equation is derived from the general equation above. The boundary energy, $\sigma_{gb}(\theta)$, is defined as a function of the angle to the interface θ.
Starting with the same energy functional:

$$f = \sum_i (W_i(\eta_1 ... \eta_p) + \frac{1}{2}\kappa(\theta)||\nabla\eta_i||^2 + \beta C) \tag{2.12}$$

the normal angle to the interface for each phase (θ_i) is computed as

$$\theta_i = \tan^{-1}(\frac{\eta_{i,2}}{\eta_{i,1}}). \tag{2.13}$$

The variational derivative of the functional becomes the following

$$\begin{aligned}\frac{\delta\eta_i}{\delta t} = &-L\Big(\mu\Big(\eta_i^3 - \eta_i + 2\gamma_i\eta_i\sum_{i\neq j}\eta_j^2\Big) - \Big(\kappa(\theta_i)\Delta\eta_i + \kappa'(\theta_i)(\boldsymbol{b}\cdot H\,\boldsymbol{n}) + \kappa''(\theta_i)(\boldsymbol{b}\cdot H\,\boldsymbol{b})\Big)\\ &+ \beta\Big(sin(\theta_i)^4\eta_{1111} - 4sin(\theta_i)^3\cos(\theta_i)\eta_{1112} + 6\sin(\theta_i)^2\cos(\theta_i)^2\eta_{1122} -\\ &4\sin(\theta_i)\cos(\theta_i)^3\eta_{1222} + \cos(\theta_i)^4\eta_{2222}\Big)\Big)\end{aligned} \tag{2.14}$$

The detailed derivation is in Appendix B. Equation 2.14, although it includes 4th order derivatives is easily evaluated in any point of the domain. To test the model only expressions for $\sigma_{gb}(\theta_i)$ and values for the other field parameters are needed.

CHAPTER III

COMPUTATIONAL IMPLEMENTETION

3.1 Grain boundary energy modeling

The objective is to simulate evolving microstructure with an *arbitrary* boundary energy function, as long as the energy function has expressions or tables for the energy and its first and second derivatives. GB energy is different for each crystalline material and configuration. In the present work two types of grain boundary models are used: one is smooth (C^∞) and one with a sharp discontinuity (C^0) that more closely mimics real GB energy. The following functional forms are used for the two energy functions

$$\sigma_{gb_I} = \sigma_0 + \sigma_1 \sin^2(2(\theta - \theta_0)), \qquad \sigma_{gb_{II}} = \sigma_0 + \sigma_1 \Big| \sin(2(\theta - \theta_0)) \Big|, \tag{3.1a}$$

$$\frac{\delta \sigma_{gb_I}}{\delta \theta} = 2\sigma_1 \sin(4(\theta - \theta_0)), \qquad \frac{\delta \sigma_{gb_{II}}}{\delta \theta} = \sigma_1 \frac{\sin(4(\theta - \theta_0))}{|\sin(2(\theta - \theta_0))|}, \tag{3.1b}$$

$$\frac{\delta^2 \sigma_{gb_I}}{\delta \theta^2} = 8\sigma_1 \cos(4(\theta - \theta_0)), \qquad \frac{\delta^2 \sigma_{gb_{II}}}{\delta \theta^2} = -4\sigma_1 \Big| \sin(2(\theta - \theta_0)) \Big|, \tag{3.1c}$$

where θ_0 is the tilt misorientation angle between the grains. Both energy functions are qualitatively similar in magnitude and shape (Figure 3.1a), and generate identical Wulff shapes (3.1b), but have very different behavior at their minima.

The boundary width ℓ_{gb} is set following the Moelans [20] criteria, that sets ℓ_{gb} to be 5 times the minimum mesh size Δx. From equations 2.14 and 2.2, the mobility m_{gb} is multiplying the all the evolution equation. The converged form of the interface is not affected by m_{gb}, therefore m_{gb} is set to 1.

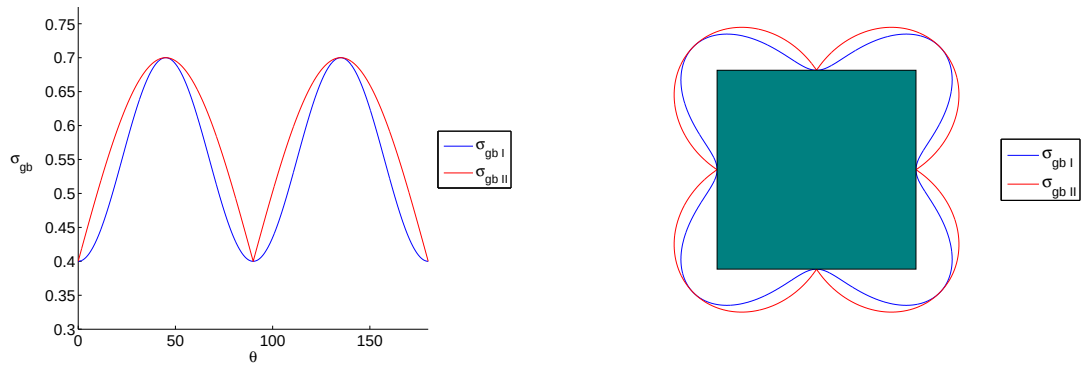

(a) Plot of both energy functions with respect to tilt angle.

(b) Wulff's construction (i.e. equilibrium crystal shape) for both energy profiles.

Figure 3.1: Comparision of smooth and nonsmooth energy functions.

3.2 Implementation

All computations are implemented and run using an in-house code called ALAMO. ALAMO uses a library called AMReX, which provides a framework for adaptive mesh refinement (AMR). AMR enables the computation to have a fine mesh only where precise calculations are needed, reducing the number of calculations and improving the performance. ALAMO refines the mesh at each time step based on the computational requirements at each point. The refinement criteria is the proximity to an interface. As bulk points do not change phase, the AMR is applied only near the interface. The numerical parameter that controls the refinement is $|\nabla\eta_i|$. For nonzero values of $|\nabla\eta_i|$, an interface is close and , therefore, refinement is needed to have more accurate calculations. This ensures that the diffuse interface is contained within the highest level of refinement (Figure 3.2).

3.3 Numerical integration and stability

An explicit numerical method was implemented to evolving the field

$$\frac{\eta_i^{n+1} - \eta_i^n}{\Delta t} \approx \frac{\delta\eta_i^n}{\delta t} \Rightarrow \eta_i^{n+1} \approx \eta_i^n + \frac{\delta\eta_i^n}{\delta t}\Delta t, \tag{3.2}$$

where $\frac{\delta\eta_i}{\delta t}$ is the result from Equation 2.14.

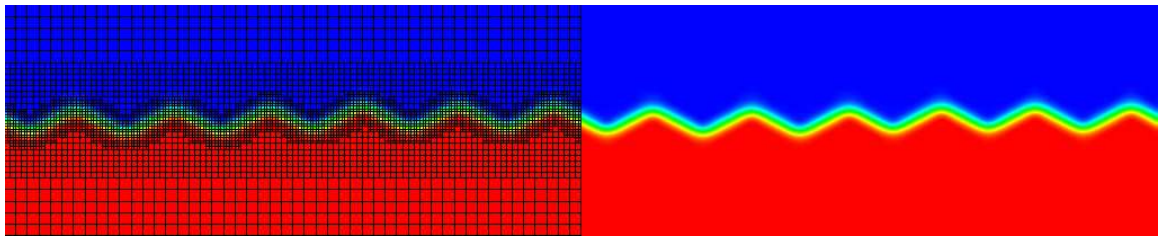

Figure 3.2: Results from a phase field test showing the 3 levels of mesh refinement, and how the interface is constrained to the finer level.

Explicit methods tend to be unstable and have the risk of overshooting the order parameters. Overshooting exist when the order parameters take values outside $[0, 1]$. Outside the bounds, the order parameters lack physical meaning. Stability of an explicit method is described with the Courant number. The Courant number (C) is a relation between the timestep (Δt), the mesh size (Δx) and the velocity (u). It can be shown that stability is guaranteed by keeping the Courant number under a certain value $C_{\max}$. The Courant number is defined as

$$C = \left|\frac{u\Delta t}{\Delta x}\right| = \left|\frac{\delta f}{\delta \eta_i}\frac{\Delta t}{\Delta x}\right| < C_{\max}. \tag{3.3}$$

In the present work, u is the rate of change of the PF order parameter $\frac{\delta f}{\delta \eta_i}$. For evolving sharp interfaces, Sun and Beckermann [34] established the criteria of $C_{\max} = 0.1$ to enforce stability of the interface. Numerical derivatives are used to evaluate the evolution equation at each point. A numerical derivative is inversely proportional to the mesh size to the power of the order of that derivative

$$\frac{\delta^i f}{\delta x^i} \propto \frac{1}{\Delta x^i}. \tag{3.4}$$

This relation is defined by the Newton's difference quotient [35].

The time step , Δt, needed for each level of refinement is different. To account for this, temporal substepping was used to reduce the number of integration steps required. For computational performance reasons, the mesh size for the finer level of refinement is restricted to the condition that $\Delta x = 0.01 << 1$. Combining Equations 3.4, 2.14 and 3.3, it is clearly seen that the term that limits the magnitude of

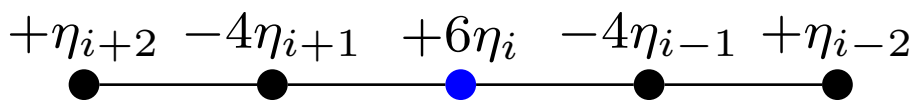

Figure 3.3: Numerical five-point stencil for a 4th order derivative .

Δt is the curvature term. This criteria is the same for the general 3D case, as the curvature term is similar and has the same magnitude. The variational derivative of curvature term has 4th order derivatives, that are extremely sensible to the mesh size. 4th order derivatives are evaluated with a 5 point numerical stencil (Figure 3.3) corresponding to the following discrete form for the derivative

$$\frac{\delta^4 \eta_i(x)}{\delta x^4} = \frac{\eta_i(x+2\Delta x) - 4\eta_i(x+\Delta x) + 6\eta_i(x) - 4\eta_i(x-\Delta x) + \eta_i(x-2\Delta x)}{\Delta x^4}. \quad (3.5)$$

From the evolution equation 2.14, where $L \approx 1$, and applying Equation 3.3, the minimum Δt such that stability is enforced becomes

$$8\frac{\beta}{\Delta x^4}\frac{\Delta t}{\Delta x} < 0.1 \Rightarrow \Delta t < \frac{0.1\Delta x^5}{8\beta}. \quad (3.6)$$

As stated in Section 3.2, ALAMO can have a different time step for each level of refinement. For each level of refinement, Δx^i is the magnitude of Δx. The refinement splits in two the cells of the prior level ($\Delta x^i = \Delta x^{i-1}/2$). Applying equation 3.6, the required Δt^i for each level of refinement is $\Delta t^i = \Delta t^{i-1}/32$. Table 3.1 illustrates the value of Δt for several values of β and Δx

3.4 Performance

The present work computes the evolution of GB in a 2D domain. As can be seen in Figure 3.2, the interface is constrained to the finer level of refinement. The evolution Equation 2.14 is 0 if evaluated far from the interface. Then, the field

		Δx			
		0.2	0.1	0.05	0.025
β	8e-4	3.2	0.1	3.13e-3	9.77e-5
	4e-4	6.4	0.2	6.25e-3	1.95e-4
	2e-4	12.8	0.4	1.25e-2	3.90e-4
	1e-4	25.6	0.8	2.5e-2	7.81e-4

Table 3.1: Δt for several values of β and Δx

only has to be evaluated in the finer
level of refinement. By evaluating
only near the interface, the scalability of the code changes. Instead of evaluating in the 2D domain, the field is evaluated along a line. When increasing the size of the domain, the number of operations will increase proportional to the interface length instead of the domain area. If L_{int} is the interface length and L_d^2 is the area of the domain

$$\#\text{operations} \propto L_{int} \approx \sqrt{L_d^2} = L_d. \tag{3.7}$$

This way of evaluating the PF is faster than most of the previous methods, and allows to work with bigger domains without a high increase of the number of computations. If AMR is not applied, using the same mesh size the number of calculations for the tests of the present work are 3 times bigger. Applying AMR and temporal substepping, the number of calculations is reduced more than a 80%.

CHAPTER IV

ANALYSIS

Processing of computational output is complex and a field of research in its own right. In this section, some of the data post-processing and analysis techniques are discussed.

4.1 Numerical interface parametrization

The visualization software package VisIt from Lawrence Berkeley National Laboratory is used for visualization of ALAMO's BoxLib output. The VisIt scripting mode is used to automate data analysis. A python driver script was written to generate a gray-scale image for each time step of ever test. This way of saving the plots allows to apply a consistent methodology for processing the images and have all the quantities obtained in the same scale and format.

With the images for all the time steps of a test, an image processing program is applied. The code includes the skimage library, used for capturing contours and discontinuities in an image. The code extracts the level curve of value 0.5 (center of the interface). The output of this process is an array with the values for the **x** and **y** axis of the interface (Figure 4.1). These arrays need to be re-dimensioned.

Figure 4.1: The original diffuse boundary (left) is processed using VisIt and results in a grayscale image (center). Python is used to parameterize the boundary characterized by the level set $\eta = 0.5$ (right).

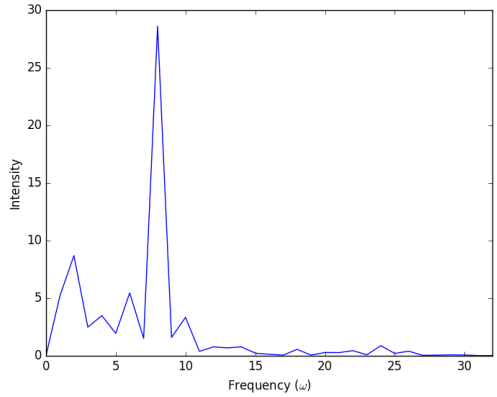

Figure 4.2: Fast Fourier transformation of the interface at a concrete time step, the higher the intensity is for a frequency, the more dominant it is on the interface.

The image processing transform the x and y axis dimensions into the pixel length in that direction. Multiplying by the rate $\frac{domain\ length}{\#pixels}$ for each dimension, the function is in the original scale.

4.2 Frequency analysis

The objective of this work is to understand the evolution in time of the interface, especially the facet frequency and shape. With that purpose in mind, an intensity chart is used to identify the dominant frequencies over time for each test. The function obtained from the image processing is not centered around 0. Having the mean value different from 0 implies a 0 frequency term. In order to avoid that noise, the mean value of the function is subtracted. A fast Fourier transform (FFT) is applied to obtain the frequencies and their intensity. The FFT transforms a function to the frequency domain (Figure 4.2). The intensity chart is generated by putting together the FFT graphs for all the time steps (Figure 4.3a). The intensity of the color shows which are the present and dominant facet frequencies at the interface in time.

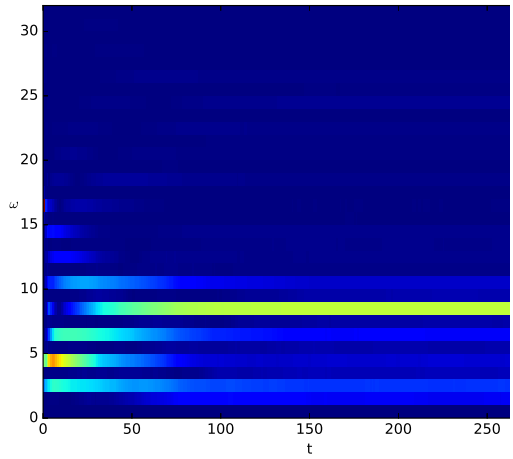

(a) Evolution of the fast Fourier transform over time, the warmer colors indicate a higher intensity of that frequency, where the cold colors indicate lower or zero presence of that frequency at the interface.

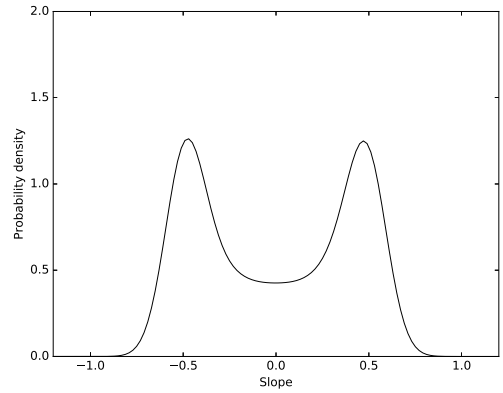

(b) Slope density chart for the converged interface of figure 4.1, the two maximum correspond to the orientation of the facets m_1 and m_2

Figure 4.3: Fourier analysis of interface convergence as a function of time.

4.3 Slope analysis

During the testing and development process of this model, it was observed that some tests with different parameters converged to the same frequency but the interfaces had different shapes. The curvature of the junctions was different and the slopes of the facets were different as well. To measure the difference between results and quantify them, a slope density analysis have been developed. The interest of the slope analysis is relevant in the converged interface, giving a measure of the junctions angles, defining their equilibrium shape. The junction angle (Θ) is obtained by determining the slope of the facets, that are the maximum values observed in the slope density chart (see Figure 4.3b) and applying the formula

$$\Theta = \tan^{-1}\left|\frac{m_1 - m_2}{1 + m_1 m_2}\right|, \tag{4.1}$$

where m_1 and m_2 are the slopes of the facets.

CHAPTER V

RESULTS

In this section the faceting behaviour of a tilt GB with an arbitrary misorientation θ_0 is studied. Annealing is the thermal process of heating a metal to 80-85 % of its melting temperature, and then cooling it. The excess of energy during the annealing process allows the boundaries to migrate to more stable (less energetic) configurations. We observe that the faceting behavior of the GB under annealing qualitatively corresponds to experimental observation (Figure 5.1). In both cases, the smooth interface with small perturbations migrated to a faceted configuration during the annealing process. The observed behavior is qualitatively similar. Realistic GB energy functions are needed to replicate the real behavior of the interface and its lengthscales. With the realistic values, the curvature energy constant β could be calibrated to match the junction frequency and slope.

5.1 Effect of boundary energy function and curvature energy

Different boundary energies, even if they have the same maximum and minimum values, imply different curvatures (Figure 5.2). This can be understood by taking the energy along a curve of the boundary energy. The total boundary energy along a curve of fixed radius is

$$\omega = \frac{(\theta_f - \theta_i)}{2\pi} 2\pi r \int_{\theta_i}^{\theta_f} \sigma_{gb} \partial\theta. \tag{5.1}$$

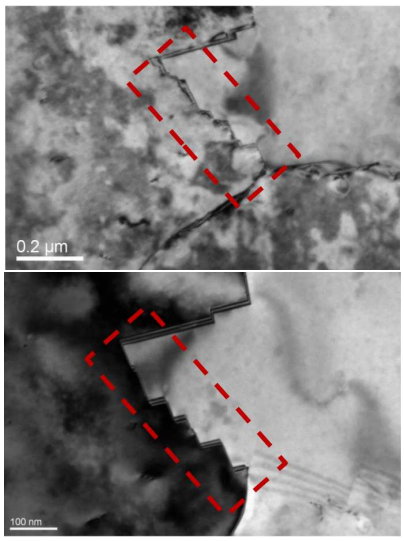

(a) In situ experimental observation of faceted microstructure in copper before and after anneal [36]

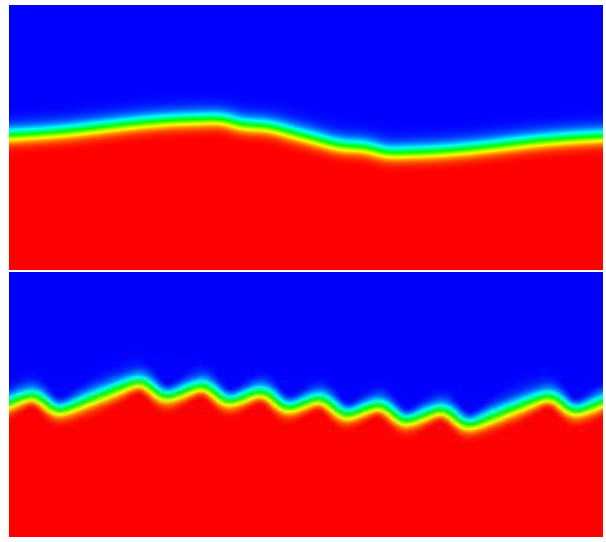

(b) ALAMO's initial condition and converged interface for time-dependent phase field evolution, with $\sigma_0 = 0.5,\ \sigma_1 = 2.0,\ \beta = 0.0004,\ l_{gb} = 0.08$.

Figure 5.1: Qualitative comparison of experimental and computational results of energy anisotropy-driven microstructure evolution. The faceting behavior of the interface under annealing is replicated.

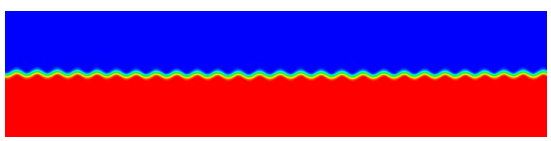

(a) $\sigma_{gb} = \sigma_0 + \sigma_1 sin(2(\theta - \theta_0))^2$

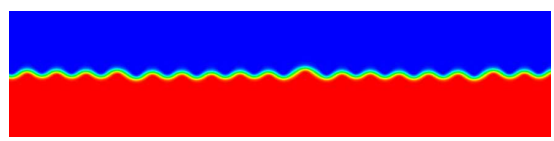

(b) $\sigma_{gb} = \sigma_0 + \sigma_1 |sin(2(\theta - \theta_0))|$

Figure 5.2: Comparison of both boundary energy functions (σ_{gb_I} and $\sigma_{gb_{II}}$) with the same magnitude for all the PF parameters, $\sigma_0 = 0.15,\ \sigma_1 = 0.95,\ \beta = 0.0001,\ \ell_{gb} = 0.05$. A difference in the facet junction curvature due to the different boundary energy is observed.

Comparing the energy associated to σ_{gb_I} and $\sigma_{gb_{II}}$ (see Section 3.1)along a curve of constant radius that connects to minimum energy facets ($\theta_i = \theta_0,\ \theta_f = \theta_0 + \pi/2$).

$$\begin{aligned}\omega_{II} - \omega_I &= \frac{\pi r}{2} \int_{\theta_0}^{\theta_0+\pi/2} \Big((\sigma_0 + \sigma_1 |sin(2(\theta - \theta_0))|) - (\sigma_0 + \sigma_1 sin(2(\theta - \theta_0))^2) \Big) \\ &= \frac{\pi r}{2}(1 - \frac{\pi}{4}) > 0. \end{aligned} \tag{5.2}$$

It can then be observed that the greater boundary energy along the curve for $\sigma_{gb_{II}}$ induces instability in the smaller facets, driving the formation of larger curvature

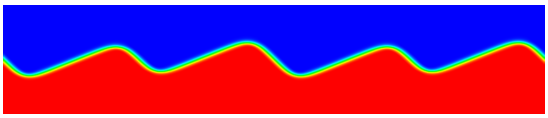

(a) $\sigma_0 = 0.015$, $\sigma_1 = 0.95$, $\beta = 8e - 4$, and $\theta_0 = \pi/6$

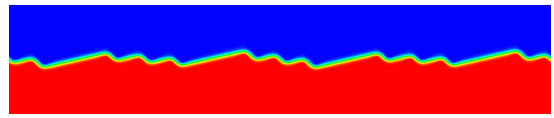

(b) $\sigma_0 = 0.015$, $\sigma_1 = 0.95$, $\beta = 8e - 4$, and $\theta_0 = \pi/6$

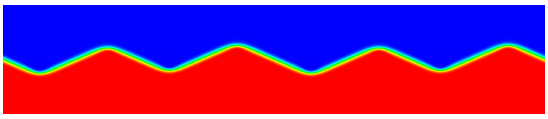

(c) $\sigma_0 = 0.015$, $\sigma_1 = 0.95$, $\beta = 8e - 4$, and $\theta_0 = \pi/4$

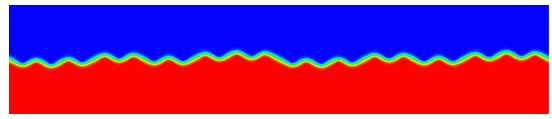

(d) $\sigma_0 = 0.015$, $\sigma_1 = 0.95$, $\beta = 8e - 4$ and $\theta_0 = \pi/4$

Figure 5.3: Interface evolution under different GB parameters. The versatility of the PF model and the variety of equilibrium configurations is observed

on the junctions (Figure 5.2).

5.2 Versatility of the PF method

The present work is not restricted to a concrete boundary energy, grain misorientation or boundary parameters (Figure 5.3). This method is general enough to adapt to any desired GB problem. The curvature associated energy parameter β can be calibrated to get the empirically observed length scale. With any desired GB energy functions and parameters, this method is able to find the equilibrium configuration of the interface under that conditions.

5.3 Evolution and convergence of the interface

The evolution of the interface over time can be observed (Figure 5.4a). As the simulation advances, the lower and higher frequencies are filtered out and the interface migrates towards the equilibrium shape. The frequency evolution is plotted over time to verify that the solution converges to one dominant frequency (Figure 5.4b).

5.4 Analysis of corner energy magnitude

The effect of the rate σ_1/β has been studied. For all the test included in the study, the boundary energy was σ_{gb_I}, and the misorientation angle $\theta_0 = \pi/4$. The slope

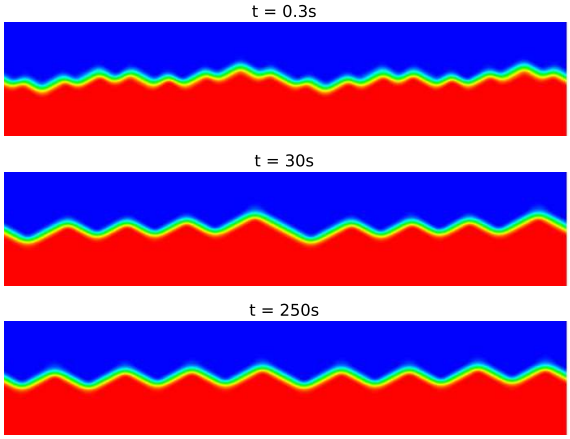

(a) Interface evolution over time, with initial frequencies $\omega_0 = \{4, 8, 32\}$, and GB parameters $l_{gb} = 0.1$, $\sigma_1 = 0.65$, $\sigma_0 = 0.015$, $\beta = 8e - 4$.

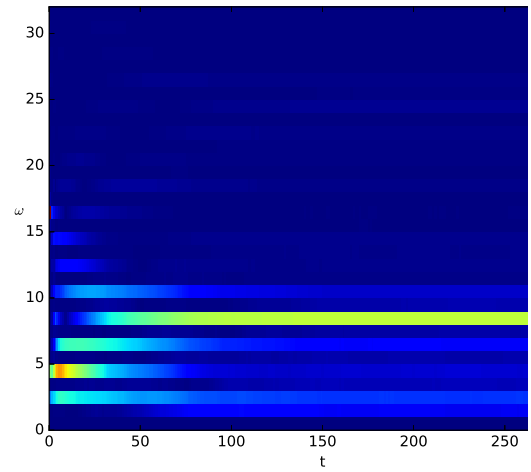

(b) Frequency chart evolution. It is observed how the high and low frequencies are filtered and the interface migrates towards an equilibrium frequency.

Figure 5.4: Spectral convergence analysis of interface indicating that the uniform facet configuration is stable.

analysis (Figures 5.5a, 5.6a and 5.7a) is a measure of the curvature of the junctions, the lower the incoming slopes the higher the radius of curvature and therefore the curve is smoother. The frequency of the converged interface for different rates σ_1/β is also analyzed (Figures 5.5b, 5.6b, 5.7b). From these results, it is not possible to get an analytical or empirical law for the facet configuration. That being said, a clear tendency to develop lower curvature and higher junction curvature as the rate σ_1/β decreases is observed.

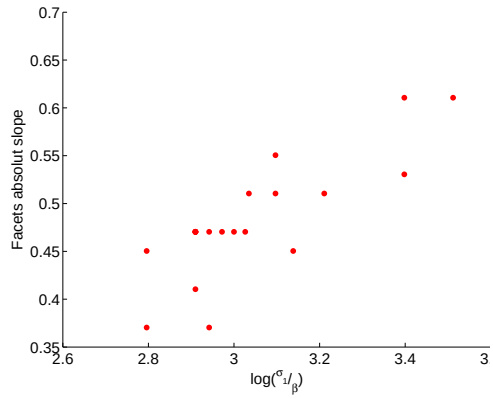

(a) Facets slope as a function of the rate σ_1/β for GB width $\ell_{gb} = 0.1$

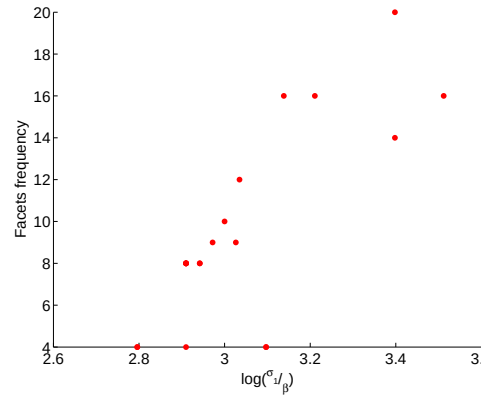

(b) Junction frequency as a function of the rate σ_1/β for GB width $\ell_{gb} = 0.1$

Figure 5.5: Analysis of the effect of the rate σ_1/β for $\ell_{gb} = 0.1$

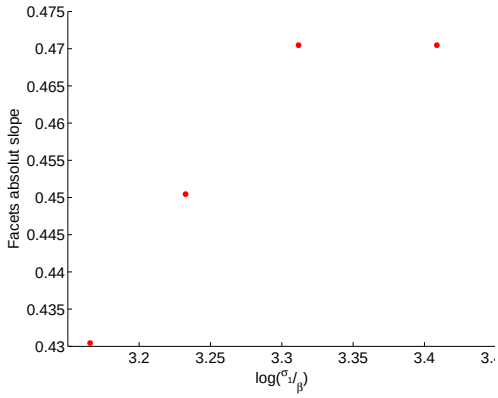

(a) Facets slope as a function of the rate σ_1/β for GB width $\ell_{gb} = 0.08$

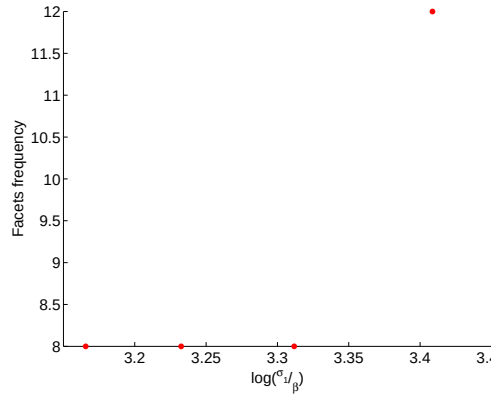

(b) Junction frequency as a function of the rate σ_1/β for GB width $\ell_{gb} = 0.08$

Figure 5.6: Analysis of the effect of the rate σ_1/β for $\ell_{gb} = 0.08$

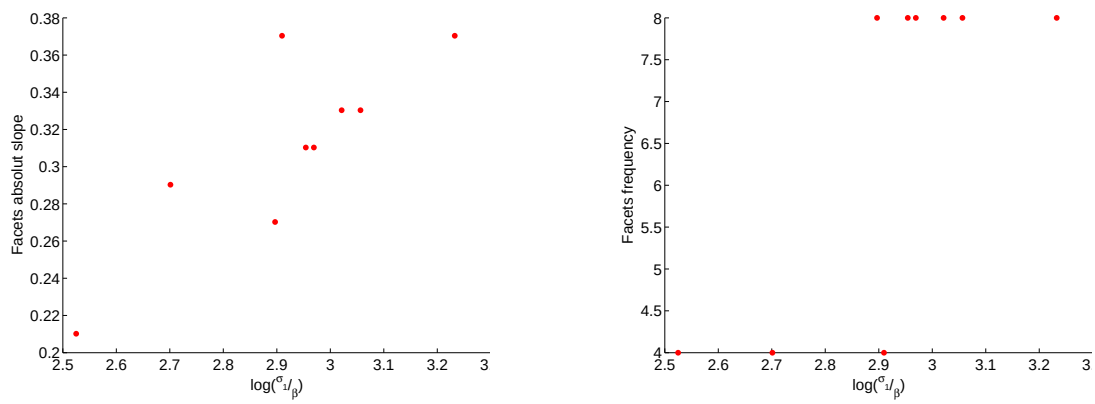

(a) Facets slope as a function of the rate σ_1/β for GB width $\ell_{gb} = 0.05$

(b) Junction frequency as a function of the rate σ_1/β for GB width $\ell_{gb} = 0.08$

Figure 5.7: Analysis of the effect of the rate σ_1/β for $\ell_{gb} = 0.1$

CHAPTER VI

CONCLUSIONS AND FUTURE WORK

6.1 Conclusions

In this work, a general anisotropic evolution equation for grain boundaries is derived, including a new way of computing second order regularization term that accounts for the facet junctions energetics. With these evolution equation, a mesoscale framework is built. The developed model is able to replicate the faceting and coarsening process of GB. The problem examined is the tilt for a generic GB energy profile. In this model class C^∞ and C^0 GB energy functions are implemented. The C^0 GB energy function has cusps (singular points with discontinuous derivatives) that are similar to the latest GB energies developed using molecular dynamics simulations and lattice-matching models [17]. The model parameters define the facet length scale and the junction, inducing an optimal frequency threshold that filters out smaller and higher frequencies. The model also captures the instability of flat interfaces oriented in non minimal directions, by inducing the faceting. In summary, the method sets an admissible domain for the curvature that corresponds to a domain of admissible frequencies for the facet junctions.

Because of its generality and versatility this model can be coupled with other phenomena, such as linear elasticity, plastic deformation, thermal deformation. This forms the basis for a possible coupling between GB energy and this processes, that will allow the effect of GB energy in these processes.

6.2 Future Work

The current computational implementation is 2D, a nontrivial 3D generalization of the computational model is required before moving to 3D. Also the model now is fed with arbitrary interfacial energy. Realistic data coming from molecular dynamics simulations should be introduced in order to generate a realistic calibration of the curvature parameter β. A PF framework to introduce linear elasticity is currently under development. This framework coupled with the present work will serve to study the effect of GB free energy in linear elastic deformation. As all computational modelling, the present work requires a validation from experimental studies. Also, the existence of a junction energy term needs to be be validated from a theoretical and experimental approach, to demonstrate that it is not just a computational tool.

REFERENCES

[1] K Kang et al. "Minimum energy structures of faceted, incoherent interfaces". In: *Journal of Applied Physics* 112.7 (2012), p. 073501.

[2] IJ Beyerlein et al. "Twinnability of bimetal interfaces in nanostructured composites". In: *Materials Research Letters* 1.2 (2013), pp. 89–95.

[3] MJ Demkowicz and L Thilly. "Structure, shear resistance and interaction with point defects of interfaces in Cu–Nb nanocomposites synthesized by severe plastic deformation". In: *Acta materialia* 59.20 (2011), pp. 7744–7756.

[4] Dmitri A Molodov, Tatiana Gorkaya, and Günter Gottstein. "Dynamics of grain boundaries under applied mechanical stress". In: *Journal of materials science* 46.12 (2011), pp. 4318–4326.

[5] Dmitri A Molodov, Tatiana Gorkaya, and Günter Gottstein. "Migration of the $\Sigma 7$ tilt grain boundary in Al under an applied external stress". In: *Scripta Materialia* 65.11 (2011), pp. 990–993.

[6] Zhang Hong-da et al. "Selective SVM ensembles based on modified BPSO". In: *Computational Intelligence and Industrial Application, 2008. PACIIA'08. Pacific-Asia Workshop on*. Vol. 1. IEEE. 2008, pp. 243–246.

[7] Jean E Taylor and John W Cahn. "Shape accommodation of a rotating embedded crystal via a new variational formulation". In: *Interfaces and Free Boundaries* 9.4 (2007), pp. 493–512.

[8] JK Chen, G Chen, and WT Reynolds Jr. "Interfacial structure and growth mechanisms of lath-shaped precipitates in Ni-45 wt Cr". In: *Philosophical Magazine A* 78.2 (1998), pp. 405–422.

[9] Wikipedia contributors. *Grain boundary — Wikipedia, The Free Encyclopedia*. [Online; accessed 5-April-2018]. 2018. URL: https://en.wikipedia.org/w/index.php?title=Grain_boundary&oldid=832166542.

[10] G Wul. "Zur Frage der Geschwindigkeit des Wachstums und der Auflosung der Kristall achen". In: *Z. Kristallogr* 34 (1901), pp. 449–530.

[11] Pierre Curie. "Sur la formation des cristaux et sur les constantes capillaires de leurs différentes faces". In: *Bull. Soc. Fr. Mineral* 8 (1885), p. 145.

[12] J Willard Gibbs. "ART. LII.–On the Equilibrium of Heterogeneous Substances". In: *American Journal of Science and Arts (1820-1879)* 16.96 (1878), p. 441.

[13] Jl Cahn and Dl Hoffman. "A vector thermodlnamics for anisotropic surfacesII. Curved and faceted surfaces". In: *Acta Metallurgica* 22.10 (1974), pp. 1205–1214.

[14] Jean E Taylor. "Crystalline variational problems". In: *Bulletin of the American Mathematical Society* 84.4 (1978), pp. 568–588.

[15] Irene Fonseca. "The Wulff theorem revisited". In: *Proceedings of the Royal Society of London A: Mathematical, Physical and Engineering Sciences*. Vol. 432. 1884. The Royal Society. 1991, pp. 125–145.

[16] TE Hsieh and RW Balluffi. "Observations of roughening/de-faceting phase transitions in grain boundaries". In: *Acta Metallurgica* 37.8 (1989), pp. 2133–2139.

[17] Brandon Runnels et al. "A relaxation method for the energy and morphology of grain boundaries and interfaces". In: *Journal of the Mechanics and Physics of Solids* 94 (2016), pp. 388–408.

[18] Bernard Dacorogna. "Weak continuity and weak lower semicontinuity of nonlinear functionals". In: *Uspekhi Matematicheskikh Nauk* 44.4 (1989), pp. 35–98.

[19] Stefan Müller. "Variational models for microstructure and phase transitions". In: *Calculus of variations and geometric evolution problems*. Springer, 1999, pp. 85–210.

[20] Nele Moelans, Bart Blanpain, and Patrick Wollants. "Quantitative phase-field approach for simulating grain growth in anisotropic systems with arbitrary inclination and misorientation dependence". In: *Physical review letters* 101.2 (2008), p. 025502.

[21] Nele Moelans, Bart Blanpain, and Patrick Wollants. "Quantitative analysis of grain boundary properties in a generalized phase field model for grain growth in anisotropic systems". In: *Physical Review B* 78.2 (2008), p. 024113.

[22] Danan Fan and L-Q Chen. "Computer simulation of grain growth using a continuum field model". In: *Acta Materialia* 45.2 (1997), pp. 611–622.

[23] A Kazaryan et al. "Grain growth in anisotropic systems: comparison of effects of energy and mobility". In: *Acta Materialia* 50.10 (2002), pp. 2491–2502.

[24] Brandon Scott Runnels. "A model for energy and morphology of crystalline grain boundaries with arbitrary geometric character". PhD thesis. California Institute of Technology, 2016.

[25] Conyers Herring. "Some theorems on the free energies of crystal surfaces". In: *Physical Review* 82.1 (1951), p. 87.

[26] William W Mullins. "Two-Dimensional Motion of Idealized Grain Boundaries". In: *Journal of Applied Physics* 27.8 (1956), pp. 900–904.

[27] Antonio Di Carlo, Morton E Gurtin, and Paolo Podio-Guidugli. "A regularized equation for anisotropic motion-by-curvature". In: *SIAM Journal on Applied Mathematics* 52.4 (1992), pp. 1111–1119.

[28] Morton E. Gurtin and Michel E. Jabbour. "Interface Evolution in Three Dimensionswith Curvature-Dependent Energy and Surface Diffusion Interface-Controlled Evolution, Phase Transitions, Epitaxial Growth of Elastic Films". In: *Archive for Rational Mechanics and Analysis* 163.3 (2002), pp. 171–208. ISSN:

1432-0673. DOI: 10.1007/s002050200193. URL: https://doi.org/10.1007/s002050200193.

[29] A.A Wheeler. "Phase-field theory of edges in an anisotropic crystal". In: *Proceedings of the Royal Society of London A: Mathematical, Physical and Engineering Sciences* 462.2075 (2006), pp. 3363–3384. ISSN: 1364-5021. DOI: 10.1098/rspa.2006.1721. eprint: http://rspa.royalsocietypublishing.org/content/462/2075/3363.full.pdf. URL: http://rspa.royalsocietypublishing.org/content/462/2075/3363.

[30] Solmaz Torabi et al. "A new phase-field model for strongly anisotropic systems". In: *Proceedings of the Royal Society of London A: Mathematical, Physical and Engineering Sciences* (2009). ISSN: 1364-5021. DOI: 10.1098/rspa.2008.0385. eprint: http://rspa.royalsocietypublishing.org/content/early/2009/02/08/rspa.2008.0385.full.pdf. URL: http://rspa.royalsocietypublishing.org/content/early/2009/02/08/rspa.2008.0385.

[31] Brian J Spencer. "Asymptotic solutions for the equilibrium crystal shape with small corner energy regularization". In: *Physical Review E* 69.1 (2004), p. 011603.

[32] Fadi Abdeljawad and Stephen M. Foiles. "Stabilization of nanocrystalline alloys via grain boundary segregation: A diffuse interface model". In: *Acta Materialia* 101.Supplement C (2015), pp. 159 –171. ISSN: 1359-6454. DOI: https://doi.org/10.1016/j.actamat.2015.07.058. URL: http://www.sciencedirect.com/science/article/pii/S1359645415005418.

[33] *A Quick and Dirty Introduction to the Curvature of Surfaces*. http://brickisland.net/cs177/?p=144. Accessed: 2018-04-06.

[34] Ying Sun and Christoph Beckermann. "Sharp interface tracking using the phase-field equation". In: *Journal of Computational Physics* 220.2 (2007), pp. 626–653.

[35] Louis Melville Milne-Thomson. *The calculus of finite differences*. American Mathematical Soc., 2000.

[36] Asher Leff et al. "Observation and modeling of minimal energy facet structures in $\Sigma 3$ and $\Sigma 9$ coppe r boundaries". In: (2018).

APPENDIX A

VARIATIONAL DERIVATIVES (3D)

The free energy functional for the GB in 3D is the following

$$\begin{aligned} F &= \int_V f(\eta_1 ... \eta_p, \nabla\eta_1, ... \nabla\eta_p, \Delta^2\eta_1, ..., \Delta^2\eta_p) dV \\ &= \int_V \sum_i (W_i(\eta_1 ... \eta_p) + \frac{1}{2}\kappa(\mathbf{n})||\nabla\eta_i||^2 + \frac{\beta}{2}C)) dV, \end{aligned} \tag{1.1}$$

where $W_i(\eta_1 ... \eta_p)$ is

$$W(\eta_1, \ldots, \eta_n) = \mu \sum_{p=1}^{n} \Big(\frac{1}{4}\eta_p^4 - \frac{1}{2}\eta_p^2 + \frac{\gamma}{2} \sum_{q \neq p} \eta_p^2 \, \eta_q^2 \Big), \tag{1.2}$$

and the curvature C is

$$C = \frac{1}{2}(\kappa_1^2 + \kappa_2^2). \tag{1.3}$$

The variational derivative have the following form

$$\frac{\delta f}{\delta \eta_i} = \frac{\partial f}{\partial \eta_i} - \frac{\partial}{\partial x_j} \frac{\partial}{\partial \eta_{i,j}} f + \frac{\partial^2}{\partial x_p \partial x_q} \frac{\partial}{\partial \eta_{i,pq}} f. \tag{1.4}$$

From the functional f the only term that depends on η_i is the chemical potential $W(\eta_1, ..., \eta_n)$, that becomes

$$\frac{\partial f}{\partial \eta_i} = \frac{\partial W}{\partial \eta_i} = \mu \Big(\eta_i^3 - \eta_i + 2\gamma_i \eta_i \sum_{i \neq j} \eta_j^2 \Big). \tag{1.5}$$

The gradient term is the only one depending on $\eta_{i,j}$, then,

$$\begin{aligned}
\frac{\partial}{\partial x_j}\frac{\partial}{\partial \eta_{i,j}} f =& \frac{\partial}{\partial x_j}\frac{\partial}{\partial \eta_{i,j}}\Big(\frac{1}{2}\kappa_i(\mathbf{n})||\nabla\eta_i||^2\Big) \\
=&\frac{\partial}{\partial x_j}\Big(\frac{1}{2}\frac{\partial \kappa_i}{\partial \mathbf{n}}\frac{\partial \mathbf{n}}{\partial \eta_{i,j}} + \kappa_i(\mathbf{n})\eta_{i,j}\Big) = \\
=&\frac{\partial}{\partial x_j}\Big(\frac{1}{2}\frac{\partial \kappa_i}{\partial \mathbf{n}}\frac{\partial \mathbf{n}}{\partial \eta_{i,j}}\Big) + \Big(\frac{\partial \kappa_i}{\partial \mathbf{n}}\frac{\partial \mathbf{n}}{\partial x_j}\eta_{i,j} + \kappa\eta_{i,jj}\Big) \\
=&\frac{\partial}{\partial x_j}\Big(\frac{1}{2}\frac{\partial \kappa_i}{\partial \mathbf{n}}\frac{\partial \mathbf{n}}{\partial \eta_{i,j}}\Big) + \frac{\partial \kappa_i}{\partial \mathbf{n}}\frac{\partial \mathbf{n}}{\partial x_j}\eta_{i,j} + \kappa\eta_{i,jj} \\
=&\frac{\partial}{\partial x_j}\Big(\frac{1}{2}\frac{\partial \kappa_i}{\partial \mathbf{n}}\frac{\partial \mathbf{n}}{\partial \eta_{i,j}}\Big) + \frac{\partial \kappa_i}{\partial \mathbf{n}}\frac{\partial \mathbf{n}}{\partial \eta_{i,j}}\frac{\partial \eta_{i,j}}{\partial x_j}\eta_{i,j} + \kappa\eta_{i,jj} \\
=&\frac{\partial}{\partial x_j}\Big(\frac{1}{2}\frac{\partial \kappa_i}{\partial \mathbf{n}}\frac{\partial \mathbf{n}}{\partial \eta_{i,j}}\Big) + \frac{\partial \kappa_i}{\partial \mathbf{n}}\frac{\partial \mathbf{n}}{\partial \eta_{i,p}}\eta_i, pj\eta_{i,j} + \kappa\eta_{i,jj}.
\end{aligned} \tag{1.6}$$

The derivations are done in the eigenbasis (see 2.2). Then $\eta_{i,pq} = 0$ if $p \neq q$, then :

$$\frac{\partial}{\partial x_j}\frac{\partial}{\partial \eta_{i,j}} f = \frac{\partial}{\partial x_j}\Big(\frac{1}{2}\frac{\partial \kappa_i}{\partial \mathbf{n}}\frac{\partial \mathbf{n}}{\partial \eta_{i,j}}\Big) + \sum_j \frac{\partial \kappa_i}{\partial n_l}\frac{\partial n_l}{\partial \eta_{i,j}}\eta_i, jj\eta_{i,j} + \kappa\eta_{i,jj} \tag{1.7}$$

Note that the normal vector components are $n_l = \frac{\nabla\eta_{i,l}}{\sqrt{\eta_{i,m}\eta_{i,m}}}$, then,

$$\frac{\partial \kappa_i}{\partial \eta_{,j}} = \frac{\partial \kappa_i}{\partial n_s}\frac{\partial n_s}{\partial \eta_{,j}} = \frac{\partial \kappa_i}{\partial n_s}\Big(\frac{\delta_{sj}\sqrt{\eta_{i,k}\eta_{i,k}} - \frac{\eta_{i,s}\eta_{i,j}}{\sqrt{\eta_{i,m}\eta_{i,m}}}}{\eta_{i,p}\eta_{i,p}}\Big) \tag{1.8}$$

Applying equation 1.8 into 1.7 , then:

$$\frac{\partial}{\partial x_j}\frac{\partial}{\partial \eta_{i,j}} f = \frac{\partial}{\partial x_j}\Big(\frac{1}{2}\frac{\partial \kappa_i}{\partial \mathbf{n}}\frac{\partial \mathbf{n}}{\partial \eta_{i,j}}\Big) + \sum\Big(\frac{\partial \kappa_i}{\partial n_j}(n_j - n_j^2\sum_p n_p)\eta_{i,jj}\Big) + \kappa_i\eta_{i,jj} \tag{1.9}$$

Knowing that the curvature is the only term depending on η_i, pq,

$$\frac{\partial^2}{\partial x_p \partial x_q}\frac{\partial}{\partial \eta_{i,pq}} f = \beta(\eta_{i,2222} + \eta_{i,3333}). \tag{1.10}$$

Adding all the terms we end up with the evolution equation for the 3D case

$$\begin{aligned}\frac{\delta\eta_i}{\delta t} =& - L\Big(\mu\Big(\eta_i^3 - \eta_i + 2\gamma_i\eta_i \sum_{i\neq j}\eta_j^2\Big) - \Big(\frac{\partial}{\partial x_j}\Big(\frac{1}{2}\frac{\partial\kappa_i}{\partial\mathbf{n}}\frac{\partial\mathbf{n}}{\partial\eta_{i,j}}\Big) \\ &+ \sum\Big(\frac{\partial\kappa_i}{\partial n_j}(n_j - n_j^2\sum_p n_p)\eta_{i,jj}\Big) + \kappa_i\eta_{i,jj}\Big) + \beta\Big(\eta_{i,2222} + \eta_{i,3333}\Big)\Big). \qquad (1.11)\end{aligned}$$

APPENDIX B

VARIATIONAL DERIVATIVES (2D)

Starting with the functional

$$f = \sum_i (W_i(\eta_1 ... \eta_p) + \frac{1}{2}\kappa(\theta)||\nabla \eta_i||^2 + \beta C) \tag{2.1}$$

where $W_i(\eta_1 ... \eta_p)$ is

$$W(\eta_1, \ldots, \eta_n) = \mu \sum_{p=1}^{n} \Big(\frac{1}{4}\eta_p^4 - \frac{1}{2}\eta_p^2 + \frac{\gamma}{2} \sum_{q \neq p} \eta_p^2 \, \eta_q^2 \Big), \tag{2.2}$$

and the curvature C is

$$C = \frac{1}{2}(\kappa_1^2) = \frac{1}{2}(\lambda_1^2). \tag{2.3}$$

The variational derivative have the following form

$$\frac{\delta f}{\delta \eta_i} = \frac{\partial f}{\partial \eta_i} - \frac{\partial}{\partial x_j} \frac{\partial}{\partial \eta_{i,j}} f + \frac{\partial^2}{\partial x_p \partial x_q} \frac{\partial}{\partial \eta_{i,pq}} f. \tag{2.4}$$

From the functional f the only term that depends on η_i is the chemical potential $W(\eta_1, ..., \eta_n)$, that becomes

$$\frac{\partial f}{\partial \eta_i} = \frac{\partial W}{\partial \eta_i} = \mu \Big(\eta_i^3 - \eta_i + 2\gamma_i \eta_i \sum_{i \neq j} \eta_j^2 \Big). \tag{2.5}$$

The gradient term is the only one depending on $\eta_{i,j}$, then,

$$\begin{aligned}\frac{\partial}{\partial x_j}\frac{\partial f}{\partial \eta_{i,j}} =& \frac{\partial}{\partial x_j}\frac{\partial}{\partial \eta_{i,j}}\Big(\frac{1}{2}\sum_i \kappa_i(\theta_i)\eta_{i,k}\eta_{i,k}\Big) = \\ =& \kappa_i(\theta)\eta_{i,jj} + \frac{\partial \kappa_i(\theta)}{\partial x_j}\eta_{i,j} + \frac{\partial}{\partial x_j}\Big(\frac{1}{2}\frac{\partial \kappa_i(\theta)}{\partial \eta_{i,j}}\eta_{i,k}\eta_{i,k}\Big)\end{aligned} \tag{2.6}$$

To compute the gradient term we need :

$$\begin{aligned}\frac{\partial \theta_i}{\partial \eta_{i,1}} &= \frac{1}{1+(\frac{\eta_{i,2}}{\eta_{i,1}})^2}\Big(-\frac{\eta_{i,2}}{\eta_{i,1}^2}\Big) = -\frac{\eta_{i,2}}{\eta_{i,1}^2+\eta_{i,2}^2} = -\frac{\eta_{i,2}}{||\nabla \eta_i||^2}, \\ \frac{\partial \theta_i}{\partial \eta_{i,2}} &= \frac{1}{1+(\frac{\eta_{i,2}}{\eta_{i,1}})^2}\Big(\frac{1}{\eta_{i,1}}\Big) = \frac{\eta_{i,1}}{\eta_{i,1}^2+\eta_{i,2}^2} = \frac{\eta_{i,1}}{||\nabla \eta_i||^2}, \\ \frac{\partial \theta_i}{\partial x_1} &= \frac{\partial \theta_i}{\partial \eta_{i,1}}\eta_{i,11} + \frac{\partial \theta_i}{\partial \eta_{i,2}}\eta_{i,12} = \frac{\eta_{i,1}\eta_{i,12}-\eta_{i,2}\eta_{i,11}}{\eta_{i,1}\eta_{,2}+\eta_{i,2}\eta_{i,2}}, \\ \frac{\partial \theta_i}{\partial x_2} &= \frac{\partial \theta_i}{\partial \eta_{i,1}}\eta_{i,12} + \frac{\partial \theta_i}{\partial \eta_{i,2}}\eta_{i,22} = \frac{\eta_{i,1}\eta_{,22}-\eta_{i,2}\eta_{i,12}}{\eta_{i,1}\eta_{i,2}+\eta_{i,2}\eta_{i,2}}.\end{aligned}$$

After deriving the Equation 2.6 and defining the normal and the tangent vectors to the surface $\mathbf{n}, \mathbf{b}$ and the Hessian $\mathbf{H}$ the following form is obtained

$$\mathbf{n} = \begin{bmatrix}\cos\theta_i \\ \sin\theta_i\end{bmatrix}$$

$$, \mathbf{b} = \begin{bmatrix}-\sin\theta_i \\ \cos\theta_i\end{bmatrix}$$

,

$$\frac{\partial}{\partial x_j}\frac{\partial f}{\partial \eta_{i,j}} = \kappa(\theta_i)\Delta\eta_i + \kappa'(\theta_i)(\boldsymbol{b}\cdot H\,\boldsymbol{n}) + \kappa''(\theta_i)(\boldsymbol{b}\cdot H\,\boldsymbol{b}).$$

Finally, to derive the curvature term

$$C = \frac{1}{2}(\lambda_2^2) = \frac{1}{2}(\boldsymbol{b}\cdot H\,\boldsymbol{b})^2, \tag{2.7}$$

Assuming b is not dependent on x_j , the derivation of the curvature term is

$$\frac{\partial^2}{\partial x_p \partial x_q}\frac{\partial}{\partial \eta_{i,pq}} f = \Big(\sin(\theta)^4 \eta_{1111} - 4\sin(\theta)^3\cos(\theta)\eta_{1112} + 6\sin(\theta)^2 \cos(\theta)^2 \eta_{1122} - 4\sin(\theta)\cos(\theta)^3 \eta_{1222} + \cos(\theta)^4 \eta_{2222} \Big) \tag{2.8}$$

Adding all the terms we end up with the expression

$$\begin{aligned} \frac{\delta \eta_i}{\delta t} = & -L\Big(\mu\Big(\eta_i^3 - \eta_i + 2\gamma_i \eta_i \sum_{i \neq j} \eta_j^2\Big) - \Big(\kappa(\theta_i)\Delta\eta_i + \kappa'(\theta_i)(\boldsymbol{b} \cdot H\,\boldsymbol{n}) + \kappa''(\theta_i)(\boldsymbol{b} \cdot H\,\boldsymbol{b})\Big) \\ & + \beta\Big(\sin(\theta)^4 \eta_{1111} - 4sin(\theta)^3 \cos(\theta)\eta_{1112} + 6\sin(\theta)^2 \cos(\theta)^2 \eta_{1122} \\ & - 4\sin(\theta)\cos(\theta)^3 \eta_{1222} + \cos(\theta)^4 \eta_{2222} \Big)\Big). \end{aligned} \tag{2.9}$$